Debris Disks among *Kepler* Solar Rotational Analog Stars

R. Silva Sobrinho[1] , A. D. Da Costa[1,2] , B. L. Canto Martins[1,3] , I. C. Leão[1] , D. Freire da Silva[1] , M. A. Teixeira[1] ,
M. Gomes de Souza[1] , D. B. de Freitas[4] , J. P. Bravo[1,5] , M. L. Das Chagas[6] , and J. R. De Medeiros[1]

[1] Departamento de Física Teórica e Experimental, Universidade Federal do Rio Grande do Norte, Natal, RN 59072-970, Brazil; rodrigosobrinho@dfte.ufrn.br
[2] Universidade da Integração da Lusofonia Afro-Brasileira, Redenção, CE 62790-000, Brazil
[3] Observatoire de Genève, Université de Genève, Chemin des Maillettes, 51, Sauverny CH-1290, Switzerland
[4] Departamento de Física, Universidade Federal do Ceará, Campus do Pici, Fortaleza, CE 60455-900, Brazil
[5] Instituto Federal de Educação, Ciência e Tecnologia do Rio Grande do Norte, Natal, RN 59015-000, Brazil
[6] Faculdade de Física—Instituto de Ciências Exatas, Universidade Federal do Sul e Sudeste do Pará, Marabá, PA 68505-080, Brazil

Abstract

Observations of circumstellar disks provide a powerful tool for our understanding of planetary system dynamics. Analogs to the solar system asteroid belts, debris disks result from the collision of the remaining solid material of the planet formation process. Even if the presence of disks is now reported for hundreds of stars, its detection around stars similar to the Sun is still very sparse. We report the results of a search for debris disks around *Kepler* stars with surface physical parameters close to solar values, including rotation period, using observations by the *Wide-field infrared Survey Explorer*. From the entire sample of *Kepler* stars, 881 targets were identified with these parameters and only six of them (KIC 1868785, 7267949, 7435796, 10533222, 11352643, and KIC 11666436) show unambiguous infrared excess, for which we determined as debris disk physical parameters. Interestingly, the present study reveals traces of debris disks much more massive and brighter than the solar system zodiacal dust, probably resulting from recent violent collisional events, orbiting stars with ages around the solar values.

Key words: circumstellar matter – infrared: stars – stars: solar-type

Supporting material: figure set

1. Introduction

The asteroid belt in our solar system is located between Mars and Jupiter, i.e., between the inner terrestrial planets and the outer giant planets, with components presenting a large compositional diversity in size and distance from the Sun (DeMeo & Carry 2014). It contains millions of irregularly shaped bodies composed of rocks, ices, and metals with a total mass of approximately 4% of the Moon or 22% of that of Pluto. The presence of water vapor on Ceres, the largest body in the asteroid belt, and the identification of objects exhibiting apparently cometary activity yet orbiting completely within the main asteroid belt (Hsieh & Jewitt 2006) are the most outstanding recent discoveries related to this region of the solar system. Observations indicate that at the planetesimal formation stage the location of the snow line, which denotes the radius outside of which ice forms, was within the asteroid belt (e.g., Martin & Livio 2012). Indeed, previous studies claimed that the inner asteroids, closest to Earth, at a radius of about 2.2 au, were water devoid, whereas the outer asteroids, within a radius around 3.2 au, were icy objects (Abe et al. 2000). However, more recent studies indicate that asteroids are less segregated by water content than previously believed (DeMeo & Carry 2014).

Although the presence of debris disks, with asteroid belt characteristics, is now well established for hundreds of stars (Aumann et al. 1984; Weissman 1995; Chen et al. 2006; Trilling et al. 2008; Patel et al. 2014; Cotten & Song 2016), the present day literature points for a scarcity of asteroid belt

signatures around Sun-like stars (Da Costa et al. 2017; Sibthorpe et al. 2018). For instance, a recent study has shown a null detection of warm debris around solar twin stars (Da Costa et al. 2017). Given this reality, we report here a search for infrared (IR) excess, a well-established diagnostic for circumstellar debris disks, in a sample of 881 *Kepler* main-sequence stars, using observations carried out with the *Wide-field Infrared Survey Explorer* (*WISE*; Wright et al. 2010). This space mission mapped the sky at wavelengths of 3.4, 4.6, 12, and 22 μm, known as filters W1, W2, W3, and W4, offering a unique laboratory for the search for stellar mid-IR excess. The 12 and 22 μm wavelengths are very sensitive to thermal emissions from objects at temperatures comparable to the Earth, around 300 K, and to the solar system asteroid belt and interior zodiacal cloud, around 150–250 K.

Indeed, thanks the high quality of the *Kepler* photometric data, we are now able to study a new type of solar analog stars, the solar rotational analogs, namely those stars presenting atmospheric solar parameters and rotation periods similar to the Sun. The stellar sample analyzed here presents these unique characteristics, surface physical properties similar to the Sun, and a rotation period, $P_{\rm rot}$, ranging from 23 to 33 days. In Section 2 of this Letter, we describe the *WISE* and *Kepler* data used in this study. Section 3 describes the methods used in our analysis of these data. Finally, in Section 4, we present our results and discuss their implications.
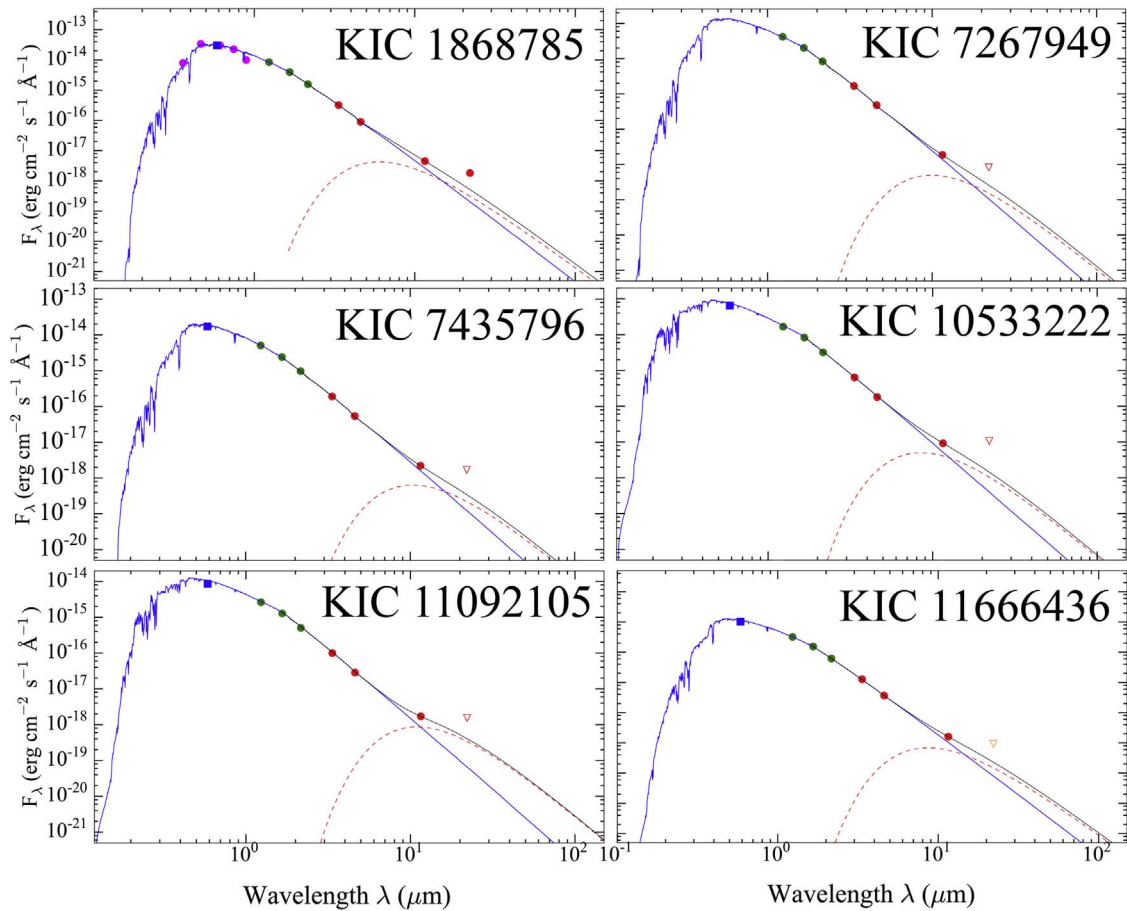
2. Stellar Working Sample and *WISE* Data Analysis

2.1. The Stellar Sample

For the present study, we use a sample of 881 *Kepler* main-sequence stars with surface physical properties close to the

Figure 1. SEDs for stars with excess IR confirmed. The blue square represents the GAIA *G*-band flux (van Leeuwen et al. 2017). The magenta, red, and green circles indicate the photometric data points from SDSS (*ugriz* filter; Abazajian et al. 2009), 2MASS (*JHK* passbands; Cutri et al. 2003), and *WISE* (Cutri et al. 2013), respectively. The blue solid line denotes the adjustment of the KURUCZ model (Castelli et al. 1997), the red dashed line corresponds to the best fit using a simple blackbody model for *WISE* bands with IR excess, and the black solid line is the sum of the two components.

solar values, that has an effective temperature in the range of $5579 \, \mathrm{K} < T_{\mathrm{eff}} < 5979 \, \mathrm{K}$, superficial gravity in the range $394 \, \mathrm{cm \, s^{-2}} < \log g < 494 \, \mathrm{cm \, s^{-2}}$, metallicity [Fe/H] ~ 0, and a rotation period P_{rot} from 23 to 33 days, namely the range of values of the rotation period of the Sun. Indeed, we have followed the same strategy as Das Chagas et al. (2016), with the rotation period P_{rot} taken from McQuillan et al. (2014).

The *Kepler* coordinates of each target were then used to cross-check with the 2MASS (Cutri et al. 2003) and full AllWISE (Cutri et al. 2013) catalogs. Assuming a positional accuracy of 5 arcsec, we find 862 stars with photometry in the three bands of 2MASS (*J*, *H*, and *K*) and in the four *WISE* bands (W1, W2, W3, and W4). The values of W3 and W4 magnitudes, SNRW3 and SNRW4 signal-to-noise ratios, and the confusion condition flag (ccf), were used as criteria to assess the quality and reliability of the *WISE* data. Checking these photometric properties, we identified 447 stars with fundamental problems such as artifact contamination (ccf = H, h, P, p, D, d, and O, o; Cutri et al. 2013), high saturation levels (W3 < 3.8 or W4 < −0.4), and very low signal-to-noise ratio (SNRW3/W4 < 2.0). We have therefore disregarded these targets from our sample. Thus, a primary sample of 415 stars with non-saturated photometry, S/N greater than 2, and unaffected by known artifacts at one or both W3 and W4 bands

was analyzed in the search for IR excess only in the band(s) in which no mentioned problem is found.

2.2. Searching for IR Excess

Then, the observed spectral energy distribution (SED) and model-derived photospheric IR fluxes for each one of the referred 415 stars were compared using the Virtual Observatory Spectral Analyzer (Bayo et al. 2008). The SEDs were constructed using the four IR bands W1–W4 from *WISE* (Cutri et al. 2013), the *J*, *H*, and *Ks* bands from 2MASS (Cutri et al. 2003), and when available, the *UBV* bands (Mermilliod 2006), the *G*-band from *Gaia* (van Leeuwen et al. 2017), and the color bands *ugriz* from the Sloan Digital Sky Survey (SDSS; Abazajian et al. 2009). To increase the reliability of the IR excess measurements, the theoretical fluxes were computed using three grids of theoretical stellar spectra: Kurucz-ATLAS9 (Castelli et al. 1997), BT-DUSTY (Allard et al. 2012), and BT-NextGen (AGSS2009; Allard et al. 2012). These models were used to determine the best fitting line for the observed data by the χ^2 minimization. Only the stars presenting IR excess from the above three models were chosen as IR excess candidates, amounting to 47 stars (see Table 2 in the online data). We also adopted the estimation of interstellar extinction provided in the *Kepler* database.
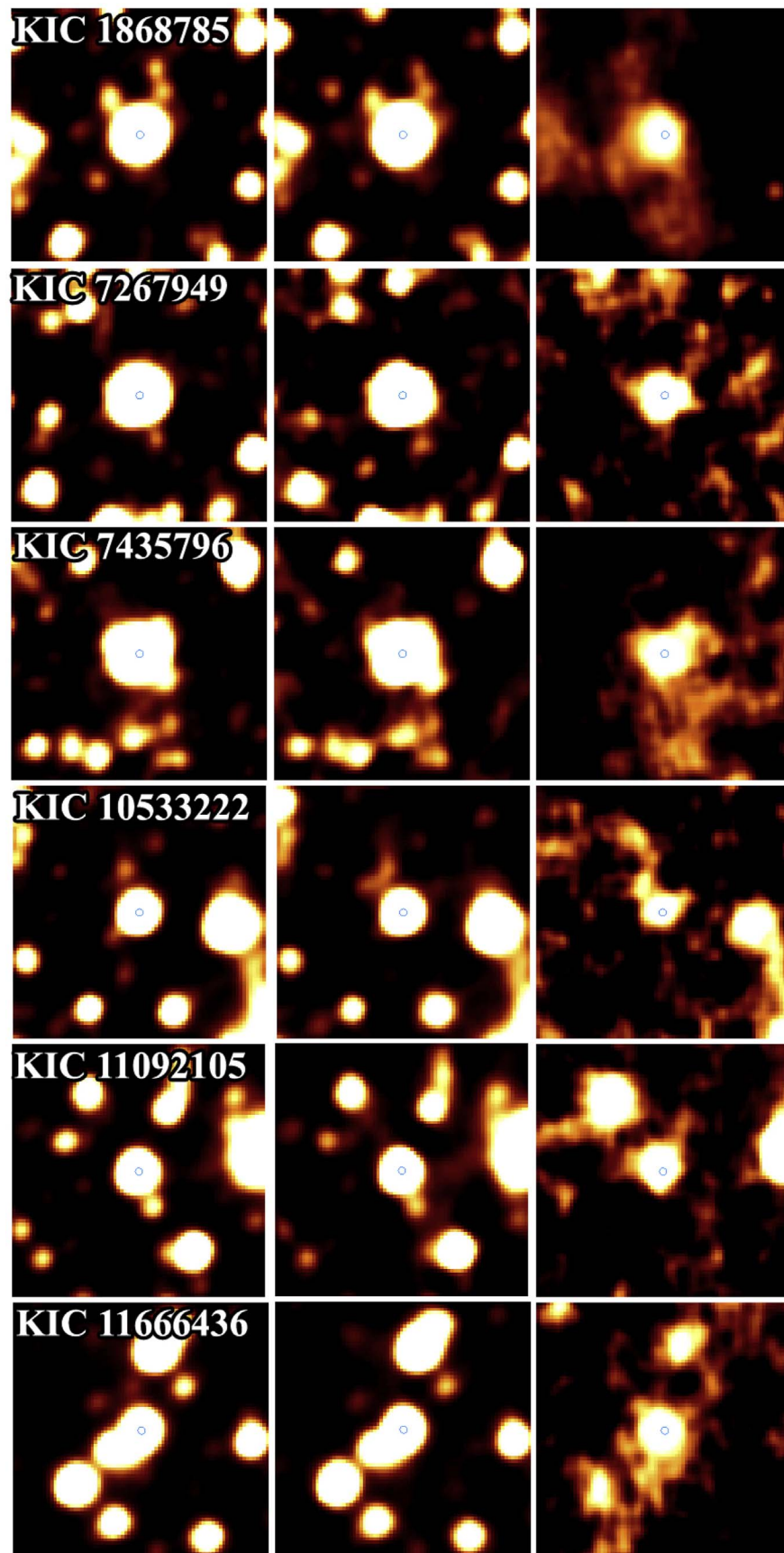
Figure 2. *WISE* images (from left to right: W1, W2, W3) for the six stars with IR excess confirmed in 12 μm, obtained from the IIRSA using 0–3σ linear scales around 1$\farcm$7 × 1$\farcm$7. No contamination by artifacts has been found in the respective bands.

Table 1
Stellar Parameters and Fundamental Disk Properties for the Sun and the Stars with Confirmed IR Excess

KIC	T_* (K)	log g (dex)	[Fe/H] (dex)	$P_{\rm rot}$ (days)	T_d (K)	R_d (au)	M_d ($M_\oplus \times 10^{-5}$)	f_d ($\times 10^{-4}$)
Sun	5777 (a)	4.44 (b)	0.00	23.0–33.5 (c)	276 (d)	<5.0 (d)	$\sim \times 10^{-4}$ (d)	$\sim 10^{-3}$ (d)
1868785	5837 ± 166	4.50 ± 0.29	-0.16 ± 0.32	24.219 ± 0.232	484 ± 22	0.33 ± 0.03	2.23 ± 0.57	19.49 ± 3.08
7267949	5629 ± 159	4.42 ± 0.13	-0.42 ± 0.36	25.109 ± 0.457	293 ± 13	0.77 ± 0.12	5.36 ± 1.98	8.26 ± 1.77
7435796	5902 ± 170	4.43 ± 0.06	0.14 ± 0.18	29.217 ± 0.362	280 ± 13	1.07 ± 0.12	12.16 ± 4.21	9.60 ± 2.21
10533222	5926 ± 176	4.29 ± 0.16	-0.12 ± 0.26	24.338 ± 0.528	341 ± 15	0.82 ± 0.15	12.32 ± 4.66	16.63 ± 3.20
11092105	5658 ± 162	4.52 ± 0.04	-0.20 ± 0.28	25.808 ± 0.429	265 ± 12	0.90 ± 0.09	23.41 ± 7.95	26.41 ± 6.23
11666436	5604 ± 155	4.56 ± 0.03	-0.20 ± 0.30	23.923 ± 0.579	336 ± 15	0.52 ± 0.05	4.07 ± 1.18	13.48 ± 2.62

Note. The stellar parameters including the effective temperature (T_*), surface gravity (log g), and metallicity ([Fe/H]) were obtained from Huber et al. (2014) and the rotation periods ($P_{\rm rot}$) were taken from McQuillan et al. (2014). The disk properties (this work) are the temperature of the dust (T_d), radius of the debris disk (R_d), dust mass of the disk of circumstellar material (M_d), and the fractional luminosity of the dust (f_d).
References. (a) Neckel (1986), (b) Gray (1992), (c) Lanza et al. (2003), (d) Roberge et al. (2012).

For quantification of the observed IR excess, we used the excess significance parameter χ_λ (Beichman et al. 2006; Moór et al. 2006), defined as

$$\chi_\lambda = \frac{F_{\lambda,{\rm obs}} - F_{\lambda,{\rm phot}}}{\sqrt{\sigma_{\lambda,{\rm obs}}^2 + \sigma_{\lambda,{\rm cal}}^2}}, \qquad (1)$$

where $F_{\lambda,{\rm obs}}$ is the observed flux density, $F_{\lambda,{\rm phot}}$ is the expected photospheric flux density, $\sigma_{\lambda,{\rm obs}}$ corresponds to the uncertainties of $F_{\lambda,{\rm obs}}$, and $\sigma_{\lambda,{\rm cal}}$ refers to the calibration uncertainties of the *WISE* data of 4.5% and 5.7% in the W3 and W4 bands, respectively (Jarrett et al. 2011). Here, only those stars for which $\chi_\lambda \geqslant 2$ (Ribas et al. 2012) are considered as presenting IR excess. This corresponds to at least a 1.5σ or 87% significance of deviation from the photosphere IR emission ($\chi_\lambda = 0.0$). Based on this criterion, we find a total of 51 stars showing *WISE* mid-IR excess, although, only 47 stars present such excess in the three theoretical models, as explained before. The difference in significance between the Kurucz and the two other models fluctuates around 10% for the W3 band and 1% for the W4 band. This fluctuation gives us an order of magnitude of the systematic errors associated to the different physical ingredients considered in each model. Our criterion of selecting objects that present excess simultaneously using different models should avoid a bias associated to a particular one (e.g., Sinclair et al. 2010). Statistical errors due to the uncertainty in the fit with the models were not taken into consideration because they are negligible. Maldonado et al. (2017) point out that, for bright objects, the *WISE* calibration error is dominant in relation to the photometric and theoretical errors. This is not the case for our sample, composed of faint objects, where the photometric error is dominant over to the *WISE* calibration errors.

2.3. WISE Image Inspection

In order to identify which stars have a reliable IR excess with no artificial artifacts or contamination we applied to the sample of 47 stars the same procedure used by Da Costa et al. (2017) for a visual inspection of the *WISE* images, based on the identification of some significant problems such as point-spread functions deformed due to an object close to the source, an absent or no evident object, or even caused by nearby objects blending, leading to a misinterpretation of the image. The *WISE* images were obtained from the Infrared Science Archive (IRSA), using 0–3σ linear scales around $1.'7 \times 1.'7$ of each IR excess candidate. In

addition, we checked if the IR excess source is a punctual (circular), elliptical (non-circular), or extensive object using a roundness criterion based on Cotten & Song (2016), which consists of a comparison of bilateral symmetry of each source determined by a two-dimensional Gaussian adjustment defined by

$$\text{Roundness} \propto \frac{(\sigma_x - \sigma_y)}{\frac{(\sigma_x + \sigma_y)}{2}}, \qquad (2)$$

where σ_x and σ_y are the standard deviations of the Gaussian fit in the x and y-axes, respectively. We tested several stars from the literature (e.g., Cotten & Song 2016) and, as a result, we concluded that the targets considered to be circular have a roundness smaller than 0.12, whereas the non-circular objects have larger values. Applying this threshold to our sample, only six targets, KIC 1868785, KIC 7267949, KIC 7435796, KIC 10533222, KIC 11092105, and KIC 11666436, survived all of the image inspection criteria. The SEDs of the KIC 1868785, KIC 7267949, KIC 7435796, KIC 10533222, KIC 11092105, and KIC 11666436 stars and their *WISE* images are shown in Figures 1 and 2, respectively. The Appendix brings the list of stars with different problems identified from the visual inspection of the WISE images (Table 3) and an example of stars with apparent IR excesses, but presenting fundamental problems in the images, are displayed in Figure 3. Stellar parameters for the stars with confirmed IR excess are also given in the Appendix (Table 4).

3. Results

Assuming that the detected IR excess in the stars KIC 1868785, KIC 7267949, KIC 7435796, KIC 10533222, KIC 11092105, and KIC 11666436 is related to IR radiation emitted by circumstellar dust, we modeled such excess using a simple blackbody function. A grid of blackbody temperatures ranging from 50 to 500 K at interval steps of 5 K (and 1 K, when necessary) was created, and the χ^2 minimization was performed to choose the dust temperature, T_d, best fitting the observed excess, from where we obtained a temperature range of 265–484 K for the circumstellar dust.

In addition, we estimated three main dust properties, the fractional luminosity f_d, the dust radius R_d, and the dust mass M_d. The fractional dust luminosity, defined as the ratio of the luminosity from the dust to that of the star, was estimated using the relationship between dust and stellar fluxes given

by Beichman et al. (2005). Considering that the detected excess for KIC 1868785, KIC 7267949, KIC 7435796, KIC 10533222, KIC 11092105, and KIC 11666436 has a peak emission at 12 μm wavelength, the minimum fractional luminosity was estimated using values equal of 484 K, 293 K, 280 K, 341 K, 265 K, and 336 K for the dust temperature around each target, respectively, corresponding to the radiative temperature of a blackbody at 12 μm.

The disk radius or orbital R_d was computed considering the dusty material as optically thin and in thermal equilibrium with the stellar radiation field. With these considerations, and assuming that the dust grains behave similarly to a blackbody, a minimum distance for the circumstellar dust was estimated following the recipe by Backman & Paresce (1993). Finally, for the disk mass M_d estimation we applied the recipe given by Liu et al. (2014). The computed debris disks physical parameters, temperature of the dust, radius of the debris disk, total mass of the disk of circumstellar material, and the fractional luminosity of the dust are given in Table 1 together with the stellar parameters. The values of excess significance and the WISE coordinates for stars in our sample with $\chi_{12} \geqslant 2.0$ or $\chi_{22} \geqslant 2.0$, from three photospheric models considered, are listed in the Appendix (Table 2).

4. Conclusions

This study reports the discovery of six *Kepler* main-sequence stars, typically solar rotational analogs with rotation periods similar to the values of the Sun, presenting mid-IR excess compatible with the presence of debris disks. The dust temperatures obtained from the modeled IR excess range from 265 to 484 K, suggesting the presence of warm circumstellar material. The computed dust parameters shows that the detected disks are located between 0.33 and 1.07 au, at smaller orbital radii than the solar system asteroid belt, that is from 2.0 and 3.5 au (Wyatt 2008). The computed temperatures indicate that the referred stars with IR excess present warm circumstellar dust with temperatures, on average, higher than the solar asteroid belt value. In effect, our findings may also represent an observational bias by considering that the presence of disks closer to the stars are hotter, and as a consequence, brighter if the IR excess is observed near the peak of their SEDs.

Circumstellar dust belts around main-sequence stars, as those reported in the present study, are composed of second-generation dust originated from the small-body population of planetary systems (Backman & Paresce 1993), which are mostly remnants of primordial protoplanetary disks (Hernández et al. 2007). These bodies can give fundamental information about the chemistry and evolution of protoplanetary disks and the planetary systems they form. Despite a similar physical mechanism expected in the production of the reported debris disks, our findings show that stars with physical parameters similar to the Sun, as is the case of the whole sample analyzed here, can in fact be very different from the Sun once the star and its circumstellar environment are considered, confirming previous results by Da Costa et al. (2017). Among these physical parameters, age is important for determining the presence of debris disks. In the present work, based on gyrochronology estimations (e.g., Barnes et al. 2016; Ceillier et al. 2016), the stellar ages for our *Kepler* stars range around

the solar age value, even though that range may be somewhat broad.

At the *WISE* wavelength bands we are observing the Wien-edge of the energy distributions. In this sense, the lack of an excess for the large majority of the analyzed stars does not necessarily imply the absence of circumstellar material. Indeed, the detection of IR excess, only in W3 band, is in agreement with the assumption of Liu et al. (2014) that the disk associated to this IR excess is geometrically thin, that is, confined within a small radius range, with all the dust at the same temperature. The disks reported here may in fact be spatially extended and, by consequence, similar to the solar system asteroid belt geometry. Their thin appearance may reflect the fact that only the inner edge of the disk can be detected with the present sensitivity. In addition, the absence of detection in the W4 band may be explained by its considerably narrower range in comparison to W3. This fact would indicate that the fraction of solar rotational analog stars possessing debris disks could be higher than the fraction observed here. Nevertheless, the discovered debris disks are, by far, brighter and more massive than the solar system zodiacal dust, a characteristic that allowed for their detection. In this sense, the observation of solar debris disks at the distance of the refereed stars would be well below the *WISE* sensitivity level.

The present sample of debris disks has too high of a luminosity to be explained by a steady-state collisional cascade (Wyatt 2008; Gáspár et al. 2013) and a large amount of warm dust that cannot be sustained at the estimated stellar ages (Wyatt 2008). These unusual characteristics may reflect a possible disk-sculpting mechanism resulting from violent collisional events (e.g., Zappalà et al. 2002; Kenyon & Bromley 2005, 2006; Durda et al. 2007; Raymond et al. 2009; Kral et al. 2015).

Dust belts cooler than those reported here have their imprints at longer wavelength bands, and slight or no excess in the mid-IR. Therefore, the null detection of IR excess, at the *WISE* sensitivity level, for the remaining 875 solar rotational analog stars will certainly motivate new observational studies at far-IR, submillimeter and millimeter wavebands for a better character-ization of material around these stars with a rotation period similar to that of the Sun. Furthermore, the presence of other disks structures (Wyatt 2008), in particular cold components like the *Kuiper* belt, and water ice traces, can be determined from observations in longer IR wavebands. In this sense, further observational studies are mandatory for the stars with detected IR excess announced here.

Appendix

The following informations are given in this section: the values of excess significance and the WISE coordinates for stars in our sample with $\chi_{12} \geqslant 2.0$ or $\chi_{22} \geqslant 2.0$, from three photospheric models considered (Table 2); a list of stars with different problems identified from the visual inspection of the WISE images (Table 3); an example of stars with apparent IR excesses, but presenting fundamental problems in the images (Figure 3); and the stellar parameters for the stars with confirmed IR excess (Table 4).
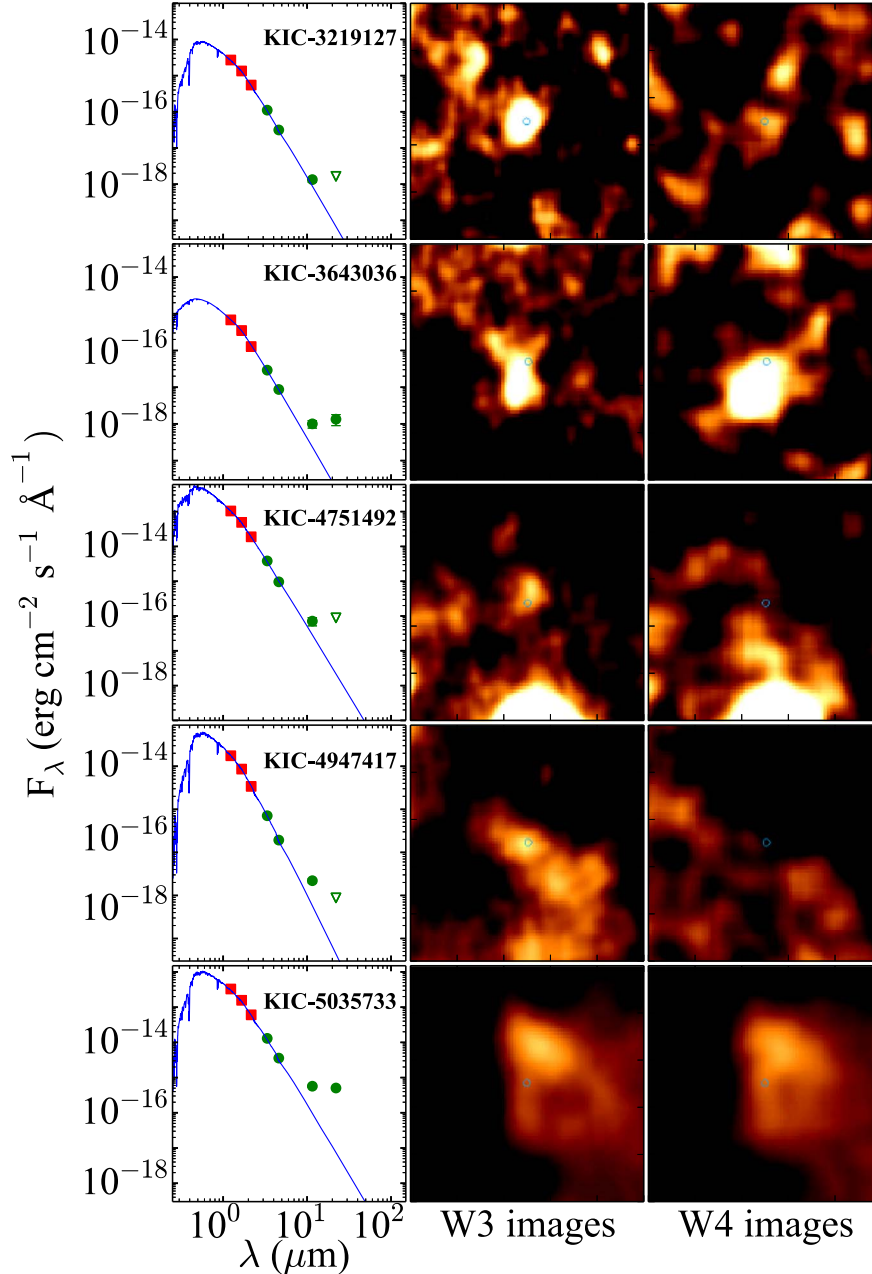
Figure 3. SEDs and *WISE* images of KIC 3219127, KIC 3643036, KIC 4751492, KIC 4947417, and KIC 5035733 stars with apparent IR excesses, but presenting fundamental problems in the images. Left panels: SED of each individual target. The red squares represent the fluxes from the 2MASS *JHK* passbands (Cutri et al. 2003). The green circles display the fluxes from the *WISE* W1–W4 bands (Cutri et al. 2003). The *WISE* upper limits are indicated by the green open triangles. The blue solid line denotes the adjustment of the Kurucz model (Castelli et al. 1997). Center/right panels: respective stellar *WISE* W3/W4 images.

(The complete figure set (9 images) is available.)

Table 2
List of the 51 Stars with IR Excess for which $\chi_{12} \geqslant 2.0$ or $\chi_{22} \geqslant 2.0$ from Three Photospheric Models: Kurucz-ATLAS9, BT-DUSTY, and BT-NextGen

KIC	R.A.	Decl.	Kurukz		NextGen		BT-Dust		Excess?	
			χ_{12}	χ_{22}	χ_{12}	χ_{22}	χ_{12}	χ_{22}	W3	W4
1868785	291.57443	37.31554	6.08	3.20	5.75	3.18	5.75	3.18	Yes	Yes
3219127	286.57025	38.39762	2.16	⋯	2.01	⋯	2.01	⋯	Yes	No
3643036	290.73413	38.71746	3.22	2.92	3.11	2.91	3.11	2.91	Yes	No
4751492	293.19486	39.88782	2.20	⋯	2.11	⋯	2.11	⋯	Yes	No
4820062	286.56364	39.96158	2.20	⋯	⋯	⋯	⋯	⋯	No	No
4947417	297.54838	40.06008	6.21	⋯	6.18	⋯	6.18	⋯	Yes	No
5035733	297.72842	40.12920	9.60	8.77	9.53	8.77	9.53	8.77	Yes	Yes
5036092	297.79665	40.18130	4.21	⋯	4.03	⋯	4.03	⋯	Yes	No
5120654	297.01951	40.21359	9.93	4.87	9.71	4.86	9.71	4.86	Yes	Yes
5198141	294.87102	40.36343	2.27	⋯	2.12	⋯	2.12	⋯	Yes	No
5263998	288.34694	40.43668	⋯	2.05	⋯	2.06	⋯	2.06	No	Yes
5293988	296.67798	40.41841	6.09	⋯	6.01	⋯	6.01	⋯	Yes	No
5428470	284.34673	40.63319	2.37	⋯	2.19	⋯	2.19	⋯	Yes	No
5534914	292.24299	40.74677	⋯	2.41	⋯	2.41	⋯	2.41	No	Yes
5730371	298.05585	40.96706	11.19	7.04	11.10	7.03	11.10	7.03	Yes	Yes
5956717	290.62853	41.29013	2.09	⋯	2.15	⋯	2.15	⋯	Yes	No
6064473	297.64333	41.30418	4.62	5.83	4.62	5.83	4.62	5.83	Yes	Yes
6142317	296.86628	41.44202	⋯	2.12	⋯	2.12	⋯	2.12	No	Yes
6345900	284.64141	41.75273	2.06	⋯	⋯	⋯	⋯	⋯	No	No
6358701	290.02545	41.72927	2.49	⋯	2.43	⋯	2.43	⋯	Yes	No
6516101	289.85597	41.90501	4.83	2.01	4.70	2.01	4.70	2.01	Yes	Yes
6952979	293.17428	42.43163	3.50	⋯	2.83	⋯	2.83	⋯	Yes	No
7267949	286.94895	42.82167	2.35	⋯	2.24	⋯	2.24	⋯	Yes	No
7435796	288.98419	43.03943	2.85	⋯	2.75	⋯	2.75	⋯	Yes	No
7457546	295.36482	43.03973	⋯	2.09	⋯	2.08	⋯	2.08	No	Yes
7763388	295.18879	43.42369	2.20	⋯	2.06	⋯	2.06	⋯	Yes	No
7772296	297.59851	43.44764	2.36	⋯	2.30	⋯	2.30	⋯	Yes	No
7953983	289.71354	43.72041	2.34	⋯	2.30	⋯	2.30	⋯	Yes	No
8042782	296.39621	43.85904	2.39	⋯	2.36	⋯	2.36	⋯	Yes	No
8328443	300.40546	44.26359	3.76	5.45	3.74	5.45	3.74	5.45	Yes	Yes
8429890	291.47401	44.48705	2.28	⋯	2.24	⋯	2.24	⋯	Yes	No
8441073	295.51828	44.44331	2.71	⋯	2.70	⋯	2.70	⋯	Yes	No
8565235	293.87219	44.64762	⋯	2.11	⋯	2.10	⋯	2.10	No	Yes
8718439	300.81718	44.82276	⋯	2.16	⋯	2.16	⋯	2.16	No	Yes
9161405	294.41346	45.55480	2.83	⋯	2.82	⋯	2.82	⋯	Yes	No
9410702	294.43354	45.91136	2.53	⋯	2.47	⋯	2.47	⋯	Yes	No
9896250	296.06648	46.72492	⋯	2.11	⋯	2.10	⋯	2.10	No	Yes
9946870	289.92768	46.85935	3.86	⋯	3.73	⋯	3.73	⋯	Yes	No
9963105	296.50230	46.87746	2.02	⋯	⋯	⋯	⋯	⋯	No	No
10468501	291.10030	47.66703	2.03	⋯	⋯	⋯	⋯	⋯	No	No
10533222	291.07269	47.71635	2.29	⋯	2.24	⋯	2.24	⋯	Yes	No
10613866	296.88037	47.81899	2.12	⋯	2.08	⋯	2.08	⋯	Yes	No
10670950	293.99346	47.95911	3.63	⋯	3.61	⋯	3.61	⋯	Yes	No
10972628	290.27466	48.48056	3.51	⋯	2.86	⋯	2.86	⋯	Yes	No
11074641	286.59790	48.63996	⋯	2.13	⋯	2.13	⋯	2.13	No	Yes
11092105	295.56162	48.64493	4.05	⋯	4.02	⋯	4.02	⋯	Yes	No
11135275	290.67574	48.72052	⋯	2.19	⋯	2.19	⋯	2.19	No	Yes
11177716	284.26121	48.88640	2.47	⋯	2.37	⋯	2.37	⋯	Yes	No
11352643	293.02650	49.18330	3.40	⋯	3.31	⋯	3.31	⋯	Yes	No
11666436	294.26457	49.73296	2.64	⋯	2.29	⋯	2.29	⋯	Yes	No
12256697	290.46572	50.93251	2.98	2.20	2.80	2.19	2.80	2.19	Yes	Yes

Note. The ellipsis (⋯) indicates upper limits for the *WISE* measurements.

Table 3
Visual Inspection of *WISE* Images for a Sample of 47 Stars with IR Excess

| KIC	Visual Inspection	Disk
1868785	Isolated single source in W3	Yes
3219127	Non-circular sources in W3	No
3643036	Offset source in W3 and W4	No
4751492	Absent source in W3	No
4947417	Absent source in W3	No
5035733	Absent source in W3 and W4	No
5036092	Offset source in W3	No
5120654	Absent source in W3 and W4	No
5198141	Confusion of sources in W3	No
5263998	Offset source in W4	No
5293988	Offset source in W3	No
5428470	Non-circular source in W3	No
5534914	Offset source in W4	No
5730371	Absent source in W3 and W4	No
5956717	Offset source in W3	No
6064473	Absent source in W3 and W4	No
6142317	Offset source in W4	No
6358701	Offset source in W3	No
6516101	Non-circular source in W3 and absent source in W4	No
6952979	Confusion of sources in W3	No
7267949	Isolated single source in W3	Yes
7435796	Isolated single source in W3	Yes
7457546	Absent source in W4	No
7763388	Non-circular source in W3	No
7772296	Absent source in W3	No
7953983	Offset source in W3	No
8042782	Offset source in W3	No
8328443	Absent source in W3 and W4	No
8429890	Absent source in W3	No
8441073	Absent source in W3	No
8565235	Absent source in W4	No
8718439	Absent source in W4	No
9161405	Absent source in W3	No
9410702	Non-circular source in W3	No
9896250	Absent source in W4	No
9946870	Non-circular source in W3	No
10533222	Isolated single source in W3	Yes
10613866	Offset source in W3	No
10670950	Confusion of sources in W3	No
10972628	Offset source in W3	No
11074641	Absent source in W4	No
11092105	Isolated single source in W3	Yes
11135275	Offset source in W4	No
11177716	Absent source in W3	No
11352643	Non-circular source in W3	No
11666436	Isolated single source in W3	Yes
12256697	Non-circular source in W3 and absent in W4	No

Table 4
Stellar Parameters for the Stars with Confirmed IR Excess

KIC	$T_*(K)$	log g	[Fe/H]	$R_*(R_\odot)$	M_* $(M_\odot)$	L_* $(L_\odot)$	$P_{\rm rot}$ (days)
1868785	5837 ± 166	4.50 ± 0.29	−0.16 ± 0.32	0.974 ± 0.079	1.083 ± 0.141	0.988 ± 0.275	24.219 ± 0.232
7267949	5629 ± 159	4.42 ± 0.13	−0.42 ± 0.36	0.900 ± 0.131	0.775 ± 0.049	0.729 ± 0.373	25.109 ± 0.457
7435796	5902 ± 170	4.43 ± 0.06	0.14 ± 0.18	1.045 ± 0.107	1.072 ± 0.129	1.188 ± 0.342	29.217 ± 0.362
10533222	5926 ± 176	4.29 ± 0.16	−0.12 ± 0.26	1.176 ± 0.209	0.976 ± 0.107	1.530 ± 0.537	24.338 ± 0.528
11092105	5658 ± 162	4.52 ± 0.04	−0.20 ± 0.28	0.852 ± 0.076	0.885 ± 0.079	0.667 ± 0.255	25.808 ± 0.429
11666436	5604 ± 155	4.56 ± 0.03	−0.20 ± 0.30	0.815 ± 0.064	0.887 ± 0.088	0.587 ± 0.222	23.923 ± 0.579

Note. Effective temperature (T_*), surface gravity (log g), metallicity ([Fe/H]), radius (R_*), and mass (M_*) were obtained from Huber et al. (2014), whereas the luminosity (L_*) was computed using these parameters. Rotation periods ($P_{\rm rot}$) were taken from McQuillan et al. (2014).

ORCID iDs

R. Silva Sobrinho ⬤ https://orcid.org/0000-0001-9158-5881
A. D. Da Costa ⬤ https://orcid.org/0000-0002-3990-8281
B. L. Canto Martins ⬤ https://orcid.org/0000-0001-5578-7400
I. C. Leão ⬤ https://orcid.org/0000-0001-5845-947X
D. Freire da Silva ⬤ https://orcid.org/0000-0003-1911-0720
M. A. Teixeira ⬤ https://orcid.org/0000-0002-5404-8451
M. Gomes de Souza ⬤ https://orcid.org/0000-0002-1591-2366
D. B. de Freitas ⬤ https://orcid.org/0000-0002-8814-6383
J. P. Bravo ⬤ https://orcid.org/0000-0002-1272-524X
M. L. Das Chagas ⬤ https://orcid.org/0000-0003-1304-6342
J. R. De Medeiros ⬤ https://orcid.org/0000-0001-8218-1586

References

Abazajian, K. N., Adelman-McCarthy, J. K., Agüeros, M. A., et al. 2009, ApJS, 182, 543
Abe, Y., Ohtani, E., Okuchi, T., Righter, K., & Drake, M. 2000, in Origin of the Earth and Moon, ed. R. M. Canup et al. (Tucson, AZ: Univ. Arizona Press), 413
Allard, F., Homeier, D., & Freytag, B. 2012, RSPTA, 370, 2765
Aumann, H. H., Beichman, C. A., Gillett, F. C., et al. 1984, ApJL, 278, L23
Backman, D. E., & Paresce, F. 1993, in Protostars and Planets III, ed. E. H. Levy & J. I. Lunine (Tucson: Univ. Arizona Press), 1253
Barnes, S. A., Weingrill, J., Fritzewski, D., Strassmeier, K. G., & Platais, I. 2016, ApJ, 823, 16
Bayo, A., Rodrigo, C., Barrado y Navascues, D., et al. 2008, A&A, 492, 277B
Beichman, C. A., Bryden, G., Rieke, G. H., et al. 2005, ApJ, 622, 1160
Beichman, C. A., Bryden, G., Stapelfeldt, K. R., et al. 2006, ApJ, 652, 1674
Castelli, F., Gratton, R. G., & Kurucz, R. L. 1997, A&A, 318, 841
Ceillier, T., van Saders, J., García, R. A., et al. 2016, MNRAS, 456, 119
Chen, C. H., Sargent, B. A., Bohac, C., et al. 2006, ApJS, 166, 351
Cotten, T. H., & Song, I. 2016, ApJS, 25, 15
Cutri, R. M., Skrutskie, M. F., van Dyk, S., et al. 2003, VizieR Online Data Catalog, 2246, 0
Cutri, R. M., Wright, E. L., Conrow, T., et al. 2013, VizieR Online Data Catalog, 2328, 0
Da Costa, A. D., Canto Martins, B. L., Leão, I. C., et al. 2017, ApJ, 837, 15
Das Chagas, M. L., Bravo, J. P., Costa, A. D., et al. 2016, MNRAS, 463, 1624
DeMeo, F. E., & Carry, B. 2014, Natur, 505, 629
Durda, D. D., Bottke, W. F., Nesvorný, D., et al. 2007, Icar, 186, 498
Gáspár, A., Rieke, G. H., & Balog, Z. 2013, ApJ, 768, 25
Gray, D. F. 1992, The Observation and Analysis of Stellar Photospheres (Cambridge: Cambridge Univ. Press)
Hernández, J., Hartmann, L., Megeath, T., et al. 2007, ApJ, 662, 1067
Hsieh, H. H., & Jewitt, D. 2006, Sci, 312, 561
Huber, D., Silva Aguirre, V., Matthews, J. M., et al. 2014, ApJS, 211, 2
Jarrett, T., Cohen, M., Masci, F., et al. 2011, ApJ, 735, 112
Kenyon, S. J., & Bromley, B. C. 2005, AJ, 130, 269
Kenyon, S. J., & Bromley, B. C. 2006, AJ, 131, 1837
Kral, Q., Thébault, P., Augereau, J.-C., Boccaletti, A., & Charnoz, S. 2015, A&A, 573, A39
Lanza, A. F., Rodonò, M., Pagano, I., et al. 2003, A&A, 403, 1135
Liu, Q., Wang, T., & Jiang, P. 2014, AJ, 148, 3
Maldonado, R. F., Chavez, M., Bertone, E., & Cruz-Saenz de Miera, F. 2017, MNRAS, 471, 3419
Martin, R. G., & Livio, M. 2012, MNRAS, 425, 6
McQuillan, A., Mazeh, T., & Aigrain, S. 2014, ApJS, 211, 24
Mermilliod, J. C. 2006, yCat, 2168, 0
Moór, A., Abrahm, P., Derekas, A., et al. 2006, ApJ, 644, 525
Neckel, H. 1986, A&A, 159, 175
Patel, R. I., Metchev, S. A., & Heinze, A. 2014, ApJS, 212, 10
Raymond, S. N., O'Brien, D. P., Morbidelli, A., & Kaib, N. A. 2009, Icar, 203, 644
Ribas, Á., Merín, B., Ardila, D. R., & Bouy, H. 2012, A&A, 541, A38
Roberge, A., Chen, C. H., Millan-Gabet, R., et al. 2012, PASP, 124, 799
Sibthorpe, B., Kennedy, G. M., Wyatt, M. C., et al. 2018, MNRAS, 475, 3046
Sinclair, J. A., Helling, Ch., & Greaves, J. S. 2010, MNRAS, 409, L49
Trilling, D. E., Bryden, G., Beichman, C. A., et al. 2008, ApJ, 674, 1086
van Leeuwen, F., Evans, D. W., De Angeli, F., et al. 2017, A&A, 599, A32
Weissman, P. R. 1995, ARA&A, 33, 327
Wright, E. L., Eisenhardt, P. R. M., Mainzer, A. K., et al. 2010, AJ, 140, 1868
Wyatt, M. C. 2008, ARA&A, 46, 339
Zappalà, V., Cellino, A., dell'Oro, A., & Paolicchi, P. 2002, in Asteroids III, ed. W. F. Bottke, Jr. et al. (Tucson, AZ: Univ. Arizona Press), 619